RSC Advances



PAPER

View Article Online
View Journal | View Issue



Cite this: *RSC Adv.*, 2024, **14**, 26166

# Large magnetic anisotropy and enhanced Curie temperature in two-dimensional $MnTe_2$ coupled with β-phase group-VA semiconductor monolayers

Wei Chen, *[a] Jujian Liao,[b] Peidong Zhu,[a] Hui Liu,[a] Zhengjian Zhu,[c] Yu Zheng[a] and Jindong Liu [d]

Promoting the Curie temperature ($T_C$) and tunning the magnetocrystalline anisotropy energy (MAE) have been key issues with two-dimensional (2D) ferromagnetic (FM) materials. Here, the structural and magnetic properties of $MnTe_2$/X (X = As, Sb and Bi) heterostructures are investigated through first-principles calculations. We reveal that monolayer $MnTe_2$ weakly interacts with monolayer As or Sb through van der Waals (vdW) forces, but has strong covalent bonds with monolayer Bi, indicated by Bi–Te bond formation. The coupling of $MnTe_2$ with these β-phase group-VA semiconductor monolayers substantially modulates MAE, with $MnTe_2$/As showing a shift to in-plane easy magnetization, and $MnTe_2$/Sb exhibiting a large perpendicular MAE of 4.13 meV per cell. The formation of vdW heterostructures influence on Te spin–orbit coupling matrix elements markedly governs MAE. $MnTe_2$/Bi also has an in-plane MAE, contributed by both Te and Bi atoms. Additionally, coupling $MnTe_2$ with X significantly affects magnetic interactions. It is worth noting that the $T_C$ of $MnTe_2$/Sb reaches 233.2 K, significantly larger than that of pure $MnTe_2$. A large perpendicular MAE and a heightened $T_C$ makes $MnTe_2$/Sb desired candidates for next-generation spintronic applications. Our work provides a way to modulate the magnetic properties of 2D FM materials.

Received 18th June 2024
Accepted 15th August 2024

DOI: 10.1039/d4ra04463k

rsc.li/rsc-advances



## I. Introduction

Ever since ferromagnetism has been observed in atomically thin $Cr(Cl/Br/I)_3$,[1–3] $Cr_2Ge_2Te_6$ (CGT)[4] and $Fe_3GeTe_2$ (FGT)[5,6] nanosheets, magnetism in two-dimensional (2D) van der Waals (vdW) materials has emerged as a focal point of research, which could drive innovation in information storage and spintronics device applications. One of the most notable advantages of 2D magnetic materials compared to bulk materials is their easily modulated magnetic properties. Studies have demonstrated that the magnetic ordering temperature, magnetic anisotropy, coercivity force and magnetization can be tuned using various methods, including the use of an electric field, strain, electrostatic doping, adsorption, ion intercalation, *etc.*[5,7–18] Additionally, owing to the absence of dangling bonds on the surfaces of 2D materials, it is feasible to stack two types of 2D materials to form vdW heterostructures.[19–22]

It is widely recognized that constructing vdW heterostructure is an effective way to tune the magnetic properties and raise Curie temperature ($T_C$) of 2D magnets,[23–34] either through the proximity effect between ferromagnetic (FM) and antiferromagnetic (AFM) materials[23] or by interfacial exchange coupling between FM and nonmagnetic materials.[24] It was reported in the experiment that the $T_C$ of FGT/$FePS_3$ and CGT/NiO heterostructures are approximately 150 K and 120 K, respectively.[23,33] Theoretical predictions indicate that both the $T_C$ and perpendicular magnetic anisotropy of the CGT/$PtSe_2$ heterostructure are considerably enhanced compared to pure CGT, owing primarily to the considerable influence of strain at the interface.[34] Moreover, the introduction of extra spin superexchange pathways in $CrI_3$/$MoTe_2$ and $PtBr_3$/$WSe_2$ heterostructures has resulted in a multiple-fold increase in the $T_C$ of their FM parent material.[24,25] VdW heterostructures significantly broaden the application of 2D magnets and are anticipated to serve as fundamental components in the development of next-generation spintronic devices.

Layered transition-metal ditellurides have garnered significant attention due to their unique properties,[35–42] including superconductivity,[35] charge density waves,[36] extremely large unsaturated magnetoresistance,[36] and the presence of Dirac and Weyl semi-metallic characteristics,[37–39] particularly in relation to magnetism.[40–42] First-principles calculations have revealed that monolayer $MnTe_2$ demonstrates FM ground states with adjustable band gaps, large magnetic moments, and high perpendicular magnetic anisotropy, making it a promising

[a]*School of Electronic Information and Electrical Engineering, Changsha University, Changsha, 410022, China. E-mail: po_ze_xi@126.com*
[b]*School of Physics and Electronics, Central South University, Changsha, 410083, China*
[c]*Hunan Weiming Energy Technology Co., Ltd, Changsha, 413500, China*
[d]*School of Physics and Electronic Information, Yantai University, Yantai, 264005, China*

contender for the development of next-generation spintronic devices.[42–45] However, the knowledge of the magnetism in $MnTe_2$-based heterostructure materials is yet to be revealed. On another note, 2D group-VA layered materials (*i.e.*, P, As, Sb, Bi) have shown a strong research interest and hold vast application prospects due to their semiconductor and stable environmental properties, positioning them as powerful contenders for future nano-devices.[26,46] Monolayers of group-VA elements exhibit various allotropes, with the highly buckled graphene-like hexagonal crystal structure (β phase) being the most stable.[46] Theoretical predictions have suggested the possibility of first-to-second-order topological phase transitions in Bi monolayers grown on the (111) surface of EuO, induced by the proximity effect.[47] Moreover, when a heavy elemental (*i.e.*, As, Sb or Bi) atomic layer is placed onto monolayer $CrI_3$, it can result in the opening of a significant bulk energy gap, realization of the quantum anomalous Hall effect (QAHE), spin reorientation, and promotion of the Curie temperature.[26,48] Motivated by these insights, we are intrigued by the potential influence of coupling the 2D $MnTe_2$ with the β-phase group-VA semiconductors (*i.e.*, As, Sb and Bi) on the magnetic properties of $MnTe_2$.

In this paper, we study the structure and the magnetic properties of the $MnTe_2$/X (X = As, Sb and Bi) heterostructures. Monolayer $MnTe_2$ weakly bonds with monolayer As or Sb by vdW interaction but strongly with monolayer Bi *via* Bi–Te covalent bonds. Coupling between the $MnTe_2$ and β-phase group-VA semiconductor monolayers notably alters the magnetic anisotropy energy (MAE) and affects magnetic interactions of $MnTe_2$. The $MnTe_2$/Sb heterostructure is noteworthy, showcasing a large perpendicular MAE of 4.13 meV, an enhanced FM coupling and a heightened Curie temperature of 233.2 K. Our finds may promote the development of novel vdW magnetic heterostructures between 2D β-phase group-VA semiconductor and magnetic materials.

## II. Computational methods

Our first-principles calculations employ density functional theory (DFT)[49] within the Vienna *ab initio* simulation package (VASP). Ion-electron interaction is described using the projector augmented wave (PAW) method,[50] while the exchange–correlation energy is handled by the Perdew–Burke–Ernzerhof (PBE) form of the generalized gradient approximation (GGA).[51] The on-site Coulomb interactions ($U$) for Mn-d orbitals are considered, with a value of 3.9 eV.[44,52,53] We have also evaluated a range of U values from 2 to 5 eV and determined that our primary conclusions remain qualitatively unchanged. The energy cutoff for plane waves is set at 500 eV, with convergence criteria ensuring that the energy difference between electronic steps and the force on each atom are less than $10^{-6}$ eV and $10^{-4}$ eV $Å^{-1}$, respectively. The first Brillouin zone for $MnTe_2$/As(Sb) and $MnTe_2$/Bi heterostructures is sampled using $\Gamma$-centered $18 \times 18 \times 1$ and $9 \times 9 \times 1$ Monkhorst–Pack grids, respectively. Gamma-centered $k$-point meshes of $15 \times 15 \times 1$ are used to calculate the energy difference between FM and AFM states in a $(2 \times 2)$ supercell. The spin–orbit coupling (SOC) effect is considered in non-collinear calculations to obtain the magnetocrystalline anisotropy energy (MAE). The energy cutoff for MAE calculations is set at 600 eV with a corresponding energy criterion of $10^{-7}$ eV. VdW correction (D3) is incorporated in all calculations to account for interactions between layers. Additionally, to prevent mirror interactions vertically, a vacuum layer of 20 Å is introduced along the $z$-direction. The magnetic transition temperature is calculated *via* Monte Carlo simulations, in which a $(80 \times 80)$ supercell is employed. The loops and the warm time are respectively set to $4 \times 10^9$ and $10^8$.

## III. Results

To begin, we performed individual lattice structure optimization for each constituent material. First-principles calculations show that monolayer $MnTe_2$ presents an octahedral T-phase characterized by the $P\bar{3}m1$ space group, as depicted in Fig. 1(a). Among the H-, T-, and T′-phases, the total energy calculations indicate that the T-phase possesses the lowest energy. In the side view, the Mn atom layer is positioned between two Te atom layers. In the top view, each Mn atom is bonded to six Te atoms, forming an octahedral configuration. The optimized lattice constant $a_0$ of monolayer $MnTe_2$ is 3.87 Å, as listed in Table 1. Monolayers of group-VA elements X (X = As, Sb and Bi) display a graphene-like hexagonal crystal structure known as the β phase, which also adopts the $P\bar{3}m1$ space group. Notably, monolayer Bi exhibits significant buckling in contrast to the other two elements. The optimized lattice constant $a_0$ of monolayer As, Sb and Bi are 3.63, 4.10 and 4.31 Å, respectively.

The $MnTe_2$/X (X = As, Sb and Bi) heterostructure is constructed by vertically stacking the $MnTe_2$ and X monolayers. To minimize the artificial internal strain caused by lattice mismatch, the $MnTe_2$/As and $MnTe_2$/Sb heterostructures are used a unit cell of monolayer As and Sb to match the primary cell of monolayer $MnTe_2$, respectively, while the $MnTe_2$/Bi heterostructure is constructed by placing a $(2 \times 2)$ supercell of monolayer $MnTe_2$ on a $(\sqrt{3} \times \sqrt{3})$ supercell of monolayer Bi, as shown in Fig. 1(b)–(d). The calculation of lattice misfit is accomplished by the formula $\varepsilon = \frac{|\alpha_1 - \alpha_2|}{\alpha_1 + \alpha_2}$, wherein $\alpha_1$ and $\alpha_2$ denote the lattice parameters of the two distinct monolayers subsequent to the process of relaxation. In the constructed $MnTe_2$/As, $MnTe_2$/Sb, and $MnTe_2$/Bi heterostructures, the lattice mismatch between monolayer As, Sb, and Bi and monolayer $MnTe_2$ is approximately 3.20%, 2.88%, and 1.92% respectively. The optimized structural data for the $MnTe_2$/X heterostructures are presented in Table 1. The optimized interlayer distances ($d_0$) for the $MnTe_2$/As and $MnTe_2$/Sb heterostructures are 3.76 Å and 3.61 Å, respectively, surpassing the sum of atomic radii at the interface, indicating the presence of vdW interaction between the two monolayers. The vdW heterostructure devices benefiting from the weak cleavage energy can be fabricated using an exfoliation-restacking technique in experiment. For $MnTe_2$/As, the As atoms are almost completely aligned with the Te atoms from the top view [see Fig. 1(b)]. In the case of $MnTe_2$/Sb, half of the Sb atoms align with Mn atoms, while the other half align with the bottom row of Te atoms in $MnTe_2$ [see Fig. 1(c)]. In contrast, the $d_0$ for the $MnTe_2$/Bi

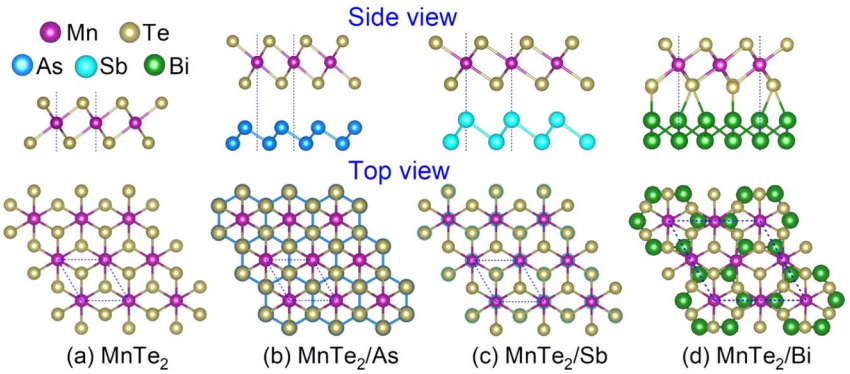


Fig. 1 Crystal structures of the (a) pure $MnTe_2$ monolayer, (b) $MnTe_2$/As, (c) $MnTe_2$/Sb and (d) $MnTe_2$/Bi heterostructures. The unit cell is denoted with dashed blue lines.

heterostructure is only about of 3.21 Å, which is less than the sum of atomic radii at the interface, suggesting a covalent bond formation between the Te and Bi atoms. To further confirm this, the Electron Localization Functions (ELF) are plotted, as shown in Fig. 2(a). For $MnTe_2$/Bi, the ELF reveals significant electron localization between Te and Bi atoms, a typical indicator of covalent bonding. On the contrary, $MnTe_2$/As and $MnTe_2$/Sb display low ELF values, indicative of weaker electron localization, consistent with vdW forces. We also take $MnTe_2$/Sb as an example and consider three different vertical stacking configurations. The energy differences between different stackings are minor, indicating their similar stability. In this context, this paper has selected the configuration with the lowest energy.

Comparing energies for four spin arrangements, one FM and three AFM arrangements (zigzag AFM (z-AFM), stripe AFM (s-AFM), and 120° noncollinear AFM (n-AFM)), as illustrated in Fig. 2(b). Our calculations reveal that the FM order exhibits enhanced energetic stability compared to the AFM configurations, and the following results are based on the FM $MnTe_2$/X heterostructure. The binding energy $E_b$ of the constructed heterostructure is calculated as $E_b = E_{MnTe_2} + E_X - E_{total}$, where $E_{MnTe_2}$, $E_X$, and $E_{total}$ are the total energies of the pure monolayer $MnTe_2$, the monolayer of group-VA element X, and the $MnTe_2$/X heterostructure, respectively. The positive binding energy values signify that all the heterostructures exhibits favorable stability. Specifically, the binding energies computed are 0.18 eV, 0.41 eV, and 1.58 eV for $MnTe_2$/As, $MnTe_2$/Sb and $MnTe_2$/Bi, respectively (see Table 1), demonstrating that monolayer $MnTe_2$ can maintain stability when interfaced with monolayer X.

Considering that $MnTe_2$/As and $MnTe_2$/Sb are vdW heterostructures, bound by weak vdW forces, in contrast to $MnTe_2$/Bi that is bonded through stronger covalent interactions, we will now discuss them separately. Compared to monolayer $MnTe_2$, the magnetic moments of the $MnTe_2$/As and $MnTe_2$/Sb heterostructures are little larger, being 3.33 $\mu_B$ and 3.35 $\mu_B$, respectively, as listed in Table 1. Fig. 3 illustrates the total density of states (TDOS) and the partial densities of states (PDOS) for each atomic orbital in monolayer $MnTe_2$ and the $MnTe_2$/X (X = As or Sb) heterostructures. The results indicate that the spin-polarized bands around the Fermi level $E_F$ primarily originate from the Mn-d local moments, whereas the contributions from the X-p and Te-p orbitals are significantly minor, meaning that the total spin moment ($S_{tot}$) is primarily contributed by the Mn atom ($S_{Mn}$). Examination of the PDOS reveals that the Mn-d states are hybridized with Te-p states, indicating some covalent character of the Mn–Te bond. If the transition metal (Mn atom in our case) is bonded to other ligands (Te atoms in our case), the five-degenerate d atomic orbitals will split in energy. Monolayer $MnTe_2$ and the $MnTe_2$/X (X = As or Sb) heterostructures all belong to the $C_{3v}$ point group. According to the ligand field theory, the Mn-d atomic orbitals are split by the crystal field into three sets: a single degenerate state ($d_{z^2}$), and two twofold degenerate states ($d_{x^2-y^2}$, $d_{xy}$) and ($d_{yz}$, $d_{xz}$). The PDOS of Mn atom shows that the Mn-d atomic orbitals are strongly exchange splitting. The five-degenerate Mn-d atomic orbitals with different orientations are delocalized owing to

Table 1 Calculated lattice constants ($a$), interlayer distances ($d$), binding energy ($E_b$), total spin moment ($S_{tot}$), magnetic moment of Mn atom ($S_{Mn}$), atom-resolved MAE of Te atom, total MAE per cell, exchange energies ($E_{ex}$), exchange constant ($J$) and Curie temperature ($T_C$)

| | | | | $S/\mu_B$ | | MAE/meV | | | | |
|---|---|---|---|---|---|---|---|---|---|---|
| System | $a$/Å | $d$/Å | $E_b$/eV | $S_{Mn}$ | $S_{tot}$ | Te | Total | $E_{ex}$/meV | $J$/meV | $T_C$/K |
| $MnTe_2$ | 3.87 | — | — | 4.19 | 3.27 | 1.28 | 1.41 | 146.6 | 2.09 | 124.6 |
| $MnTe_2$/As | 3.79 | 3.76 | 0.18 | 4.12 | 3.33 | −1.72 | −1.76 | 49.8 | 0.73 | 40.2 |
| $MnTe_2$/Sb | 4.03 | 3.61 | 0.41 | 4.21 | 3.35 | 4.16 | 4.23 | 278.6 | 3.93 | 233.2 |
| $MnTe_2$/Bi | 7.72 | — | 1.58 | 4.20 | 13.89 | −1.81 | −12.72 | 160.6 | 2.28 | 136.7 |

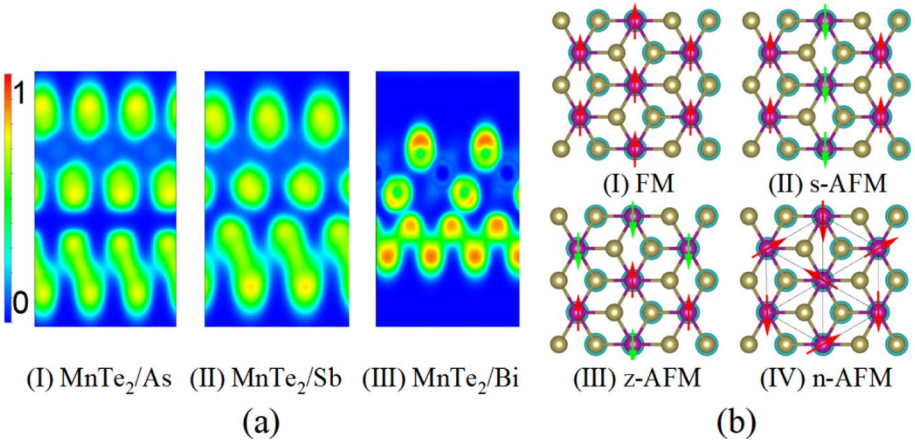


Fig. 2 (a) The Electron Localization Function (ELF) projecion on the (110) plane of the $MnTe_2$/X (X = As, Sb and Bi) heterostructures with the 0 and 1 being extremely low and highly localized charge regions, respectively. (b) Schematic diagram of ferromagnetic (FM) and three antiferromagnetic (AFM) configurations on honeycomb lattice: zigzag AFM (z-AFM), stripe AFM (s-AFM), and 120° noncollinear AFM (n-AFM).

overlap and hybridization between orbitals. According to Hund's rule and the Pauli exclusion principle, the spin-up (majority-spin) orbitals are almost totally occupied by the five unpaired $Mn^{5+}$ d electrons, while the spin-down (minority-spin) states are partially occupied, causing $S_{Mn}$ little smaller than the magnetic moment of an isolated Mn atom (the calculated value is 5 $\mu_B$). The $S_{Mn}$ in $MnTe_2$ and $MnTe_2$/X exceeding $S_{tot}$ represent the local magnetic moment of an individual Mn atom within the Wigner-Seitz radius. For the chalcogen Te atom, the three p atomic orbitals are split into one non-degenerate ($p_z$) state and one double-degenerate ($p_x$, $p_y$) state under the influence of the crystal field. The sum of the spin-down occupied states slightly exceeds that of the spin-up occupied states, leading to a minor antiferromagnetic moment contribution from the Te atom. In the case of the As atom, a near-equal occupancy of spin-down and spin-up states is observed, which does not contribute to the $S_{tot}$ of the $MnTe_2$/As heterostructure. In $MnTe_2$/Sb, Sb atom presents a higher occupancy in spin-down states compared to spin-up states, thus exhibiting a negative magnetic moment akin to that of Te. However, the consequent magnetic moment of the Sb atom is significantly lower than that of the Te atom, amounting to merely one-fourth of the magnetic moment of the later.

The MAE is calculated using GGA+U+SOC method. Self-consistent calculations are performed to obtained the total energies for in-plane and out-of-plane magnetization directions, respectively, and MAE is evaluated by the difference between the total energies for the two magnetization directions, defined as $MAE = E_{[100]} - E_{[001]}$, where $E_{[100]}$ and $E_{[001]}$ are the total energies when magnetization is in plane and normal to the plane, respectively. The negative MAE denotes the in-plane easy magnetization [100] axis and the positive one indicates their easily magnetized direction is the [001] axis. Table 1 shows the relevant data of monolayer $MnTe_2$, the $MnTe_2$/X (X = As or Sb) heterostructures, respectively. Interestingly, coupling monolayer $MnTe_2$ with a monolayer of As reorients the easy-magnetization axis from out-of-plane in monolayer $MnTe_2$ to in-plane in $MnTe_2$/As. While coupling with a monolayer of Sb greatly enhances the perpendicular MAE, from 1.41 meV per cell in monolayer $MnTe_2$ to 4.18 meV per cell in $MnTe_2$/Sb. Crucially, as shown in Table 1, the MAE of monolayer $MnTe_2$ and the $MnTe_2$/X heterostructures mainly comes from Te atoms. Quantitatively, when monolayer $MnTe_2$ is coupled with monolayer As, the contribution of the Te atom to the MAE shifts from a positive 1.28 meV to a negative −1.72 meV, the negative contribution of the Mn atom to the MAE increases a little from −0.18 meV to −0.26 meV, and the contribution of the As atom to the MAE is negligible. When monolayer $MnTe_2$ is coupled with monolayer Sb, the positive contribution of the Te atom to the MAE greatly increases, reaching up to 4.16 meV, the contribution of the Mn atom to the MAE shifts from negative to a positive 0.32 meV, and the contribution of the Sb atom to the MAE is comparable to that of the Mn atom, at 0.47 meV. To investigate whether the reorientation of the easy-magnetization direction and the increased perpendicular MAE are caused by the strain induced by the monolayers of As and Sb, respectively, we further calculate the MAEs of the stressed $MnTe_2$ monolayers with the same lattice constants as those in $MnTe_2$/As and $MnTe_2$/Sb, yielding MAEs of −1.66 meV per cell and 2.71 meV per cell, respectively. This suggests that the MAE observed in $MnTe_2$/As mainly originates from strain exerted on the $MnTe_2$ layer. Conversely, in $MnTe_2$/Sb, the total MAE cannot be exclusively ascribed to the strain effects within the $MnTe_2$ layer, a contributing factor also stems from the Sb element.

In the single-ion model, MAE results from the combined effects of the SOC of magnetic atoms and the crystal field splitting of their orbital states. Notably, previous research indicates that the SOC of heavy elements also plays a crucial role in determining MAE, as observed in materials like $CrI_3$ and $InCrTe_3$. To explore this further, we calculated the SOC contributions to MAE from each element. Fig. 4 presents the orbital-projected contributions to MAE from Mn, Te, and X atoms in monolayer $MnTe_2$ and the $MnTe_2$/X (X = As or Sb) heterostructures. It is evident that the MAE primarily comes from the

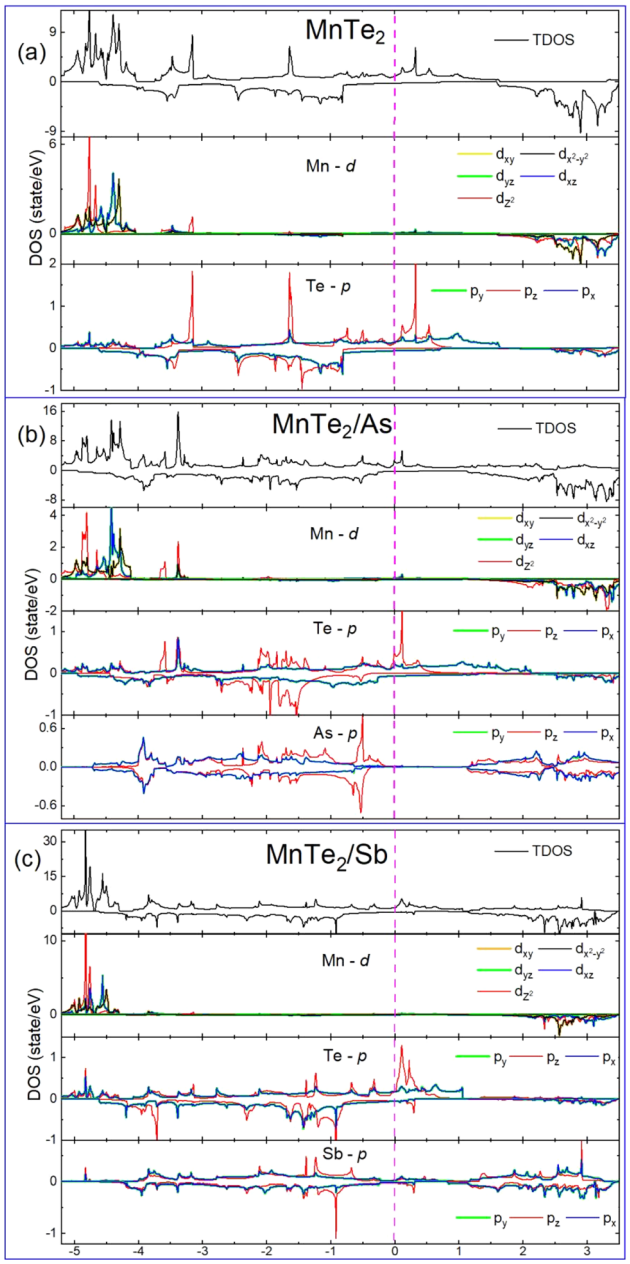


Fig. 3 Total DOS and corresponding PDOS of the (a) pure $MnTe_2$ monolayer, (b) $MnTe_2$/As and (c) $MnTe_2$/Sb heterostructures. The vertical dashed line represents the Fermi energy level which is set as zero.

contribution of the Te atom, despite its magnetic moment being much smaller than that of the Mn atom. In monolayer $MnTe_2$, the positive contribution to the MAE arises from SOC through the Te atom's ($p_z$, $p_y$) orbitals, which outweighs the negative contributions from SOC between the ($p_x$, $p_y$), resulting in a net positive MAE [Fig. 4(a)]. When coupling monolayer $MnTe_2$ with a monolayer of As, the positive contribution from SOC through the Te atom's ($p_z$, $p_y$) orbitals significantly decreases, while the negative contribution from SOC between the ($p_x$, $p_y$) markedly increases [Fig. 4(b)]. Consequently, the easy magnetization direction changes from out-of-plane in monolayer $MnTe_2$ to in-plane in $MnTe_2$/As. When coupling monolayer $MnTe_2$ with a monolayer of Sb, the contribution from SOC through the Te atom's ($p_x$, $p_y$) orbitals shifts from negative to positive, and SOC through the ($p_z$, $p_y$) also provides positive contributions [Fig. 4(c)]. As a result, $MnTe_2$/Sb exhibits a larger perpendicular MAE than monolayer $MnTe_2$. Examining the contributions from the orbitals of the Mn and X atoms reveals nuanced impacts on the total MAE. The above results show that the formation of the heterostructure predominantly affects the SOC matrix element difference of Te atoms, which in turn regulates the magnetic anisotropy of the heterostructure.

By comparing the PDOS of monolayer $MnTe_2$ and the $MnTe_2$/X (X = As or Sb) heterostructures in Fig. 3, we can qualitatively knowledge the reasons for the changes in the MAE contribution from Te atoms. Within the energy range of −1 to 0 eV around the Fermi level, the Te PDOS shows distinct characteristics. In $MnTe_2$/As, the spin-down ($p_x$, $p_y$) states of the Te atom are closer to the Fermi level compared to those in monolayer $MnTe_2$, wherein these states are slightly further away. In contrast, for $MnTe_2$/Sb, the Te PDOS almost only displays the spin-up ($p_x$, $p_y$) states in the same energy span. Consequently, the contribution of the Te atom's ($p_x$, $p_y$) orbitals to the MAE is smaller in monolayer $MnTe_2$ than that in $MnTe_2$/As, shifting from a negative value in monolayer $MnTe_2$ to a positive value in $MnTe_2$/Sb. Further examining the $p_z$ states of Te, both monolayer $MnTe_2$ and the $MnTe_2$/Sb heterostructure exhibit significant spin-down $p_z$ states within the −1 to 0 eV range around the Fermi level, while the spin-down $p_z$ states are absent in $MnTe_2$/As. Therefore, the MAE contribution from the Te atom's ($p_z$, $p_y$) orbitals in $MnTe_2$/As is further smaller than that in $MnTe_2$ and $MnTe_2$/Sb.

Next, we examine the magnetic properties of the $MnTe_2$/Bi heterostructure. Given that the SOC of heavy Bi atoms may significantly influence the MAE and exchange coupling, we conduct a detailed magnetic analysis. The calculated magnetic moment of $MnTe_2$/Bi is 13.87 $\mu_B$, which is a little larger than that of a (2 × 2) $MnTe_2$ supercell. The TDOS and PDOS of $MnTe_2$/Bi [see Fig. 5(a)] show that the magnetic moment is mainly contributed by the Mn atoms. Specifically, each Mn atom contributes an average of about 4.20 $\mu_B$, while each Te and Bi atom contributes an average magnetic moment of −0.27 $\mu_B$ and −0.10 $\mu_B$, respectively. The magnetic moments of the Te and Bi atoms changes oppositely to the Mn atoms, suggesting antiferromagnetic coupling between them. Examination of the PDOS reveals an evident hybridization between the Te-p and Bi-p states, indicating some covalent-like component of the Bi–Te bond, further suggesting that the layers of $MnTe_2$ and Bi are coupled through covalent bonds.

Fig. 5(b) presents the orbital-projected contributions to MAE from Mn, Te, and Bi atoms in $MnTe_2$/Bi. It is evident that the MAE primarily comes from the contribution of the heavy Te and Bi elements. Specifically, each Mn, Te, and Bi atom contribute −0.22 meV, −1.81 meV, and −1.39 meV to the negative MAE, respectively, resulting in a total MAE of −12.72 meV for $MnTe_2$/Bi. The Mn MAE in $MnTe_2$/Bi are almost equal to that in monolayer $MnTe_2$, while the Te MAE shifts from positive to negative. This may be attributed to the formation of the Bi–Te covalent bonds when coupling monolayer $MnTe_2$ with

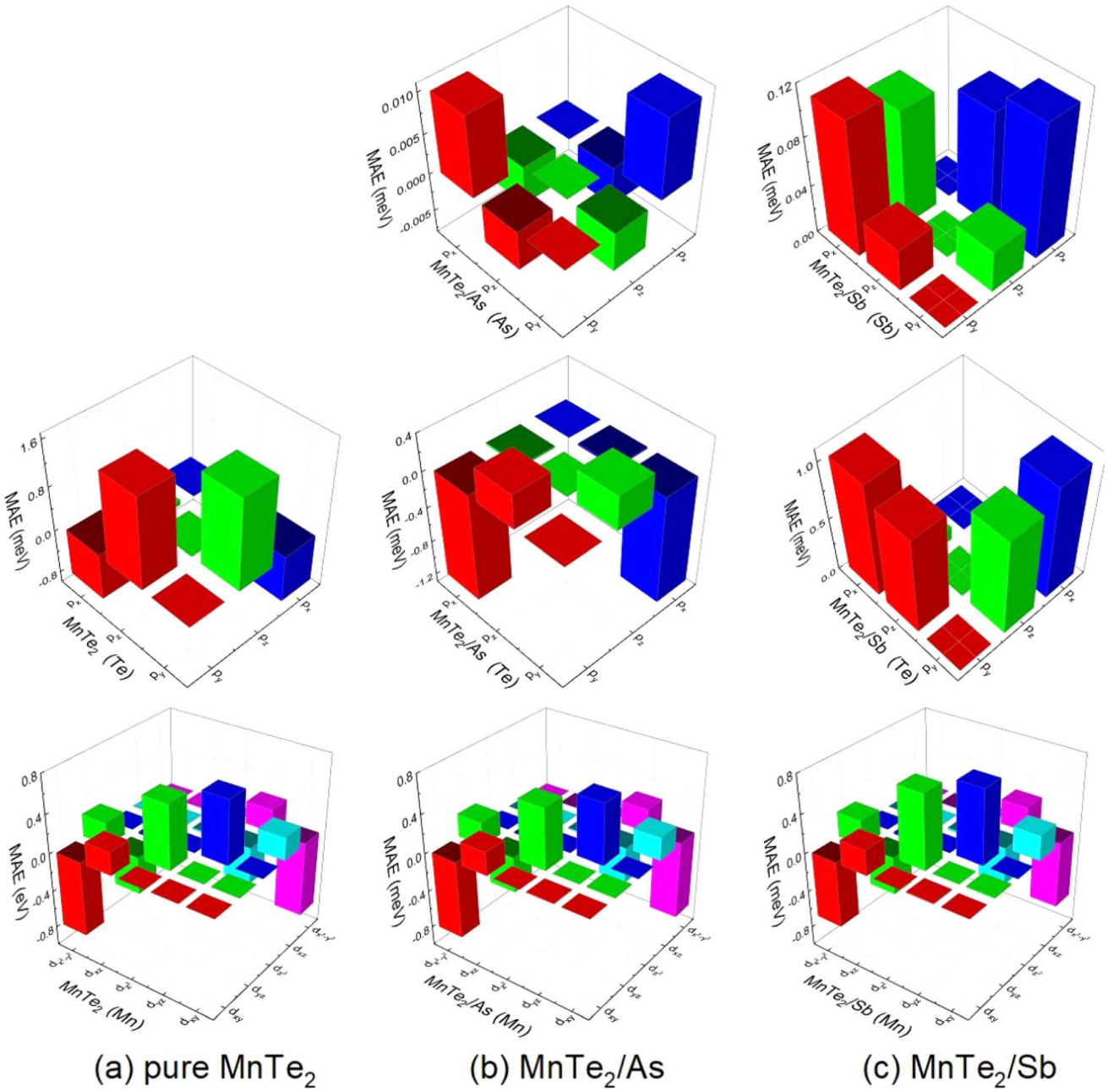


Fig. 4 Orbital-projected contribution to MAE from the SOC interaction for As and Sb (the upper row), Te (the middle row) and Mn (the bottom row) atoms in the pure $MnTe_2$ monolayer, the $MnTe_2$/As and $MnTe_2$/Sb heterostructures.

a monolayer of Bi, as shown in Fig. 1(d). Comparing Fig. 3(a) with Fig. 5(a) reveals that the PDOS of the Mn atoms in the pure $MnTe_2$ monolayer and the $MnTe_2$/Bi heterostructure remain largely unaffected, while the PDOS of the Te atoms exhibits significant changes. For example, within the −1 to 0 eV range near the Fermi level, the Te atoms in $MnTe_2$/Bi show a near-equal occupancy of the spin-down and spin-up ($p_x$, $p_y$) states, in contrast to the pure $MnTe_2$ monolayer. Additionally, the spin-down $p_z$ states are nearly absent in $MnTe_2$/Bi, unlike in the pristine monolayer. As a result of forming the $MnTe_2$/Bi heterostructure, the orbital contribution to the MAE from the Mn remains almost unchanged, whereas there is a substantial variation in the orbital contributions from the Te atoms to the MAE. Moreover, Fig. 5(b) shows that the Te MAE comes from the ($p_z$, $p_y$) orbitals, and the Bi MAE mainly arises from the ($p_x$, $p_y$) and ($p_z$, $p_y$) orbitals.

To elucidate the charge transfer between $MnTe_2$ and the substrates, we employed Bader charge analysis which provides insights into the bonding interaction between the two. Specifically, on average, each As atom in the $MnTe_2$/As heterostructure transfers a modest 0.00562 e to the $MnTe_2$ layer. The $MnTe_2$/Sb heterostructure is characterized by an average transfer of 0.03230 e per Sb atom, indicating a more substantial charge movement. In the $MnTe_2$/Bi heterostructure, each Bi atom

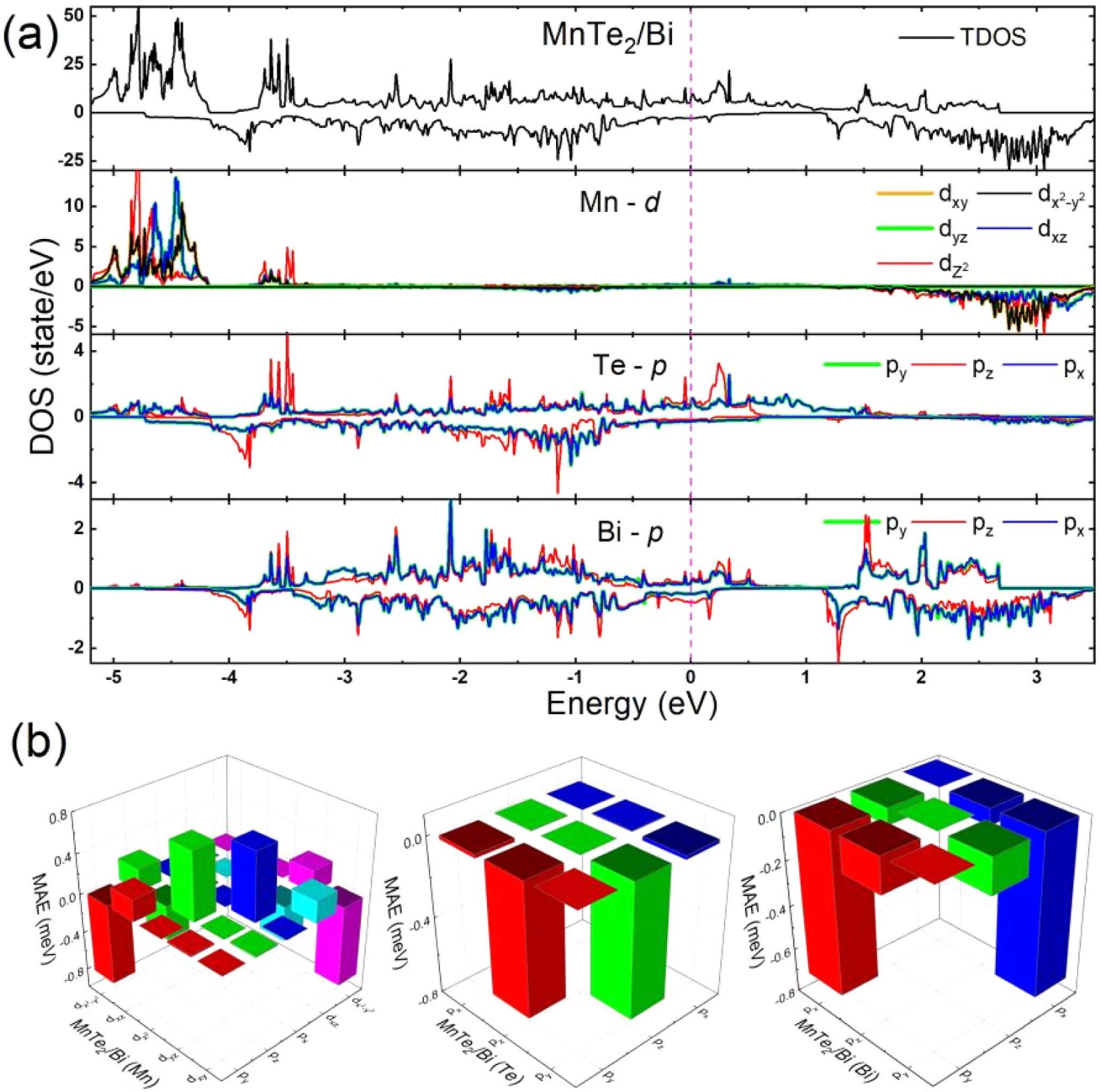


Fig. 5 (a) The TDOS and corresponding PDOS of the $MnTe_2$/Bi heterostructure. The vertical dashed line represents the Fermi energy level which is set as zero. (b) Orbital-projected contribution to MAE from the SOC interaction for Mn, Te and Bi atoms in the $MnTe_2$/Bi heterostructure.

contributes an average of 0.06956 e. This considerable charge transfer underscores the covalent Bi–Te bond formation.

The exchange interaction and the Curie temperature of the $MnTe_2$/X (X = As, Sb and Bi) heterostructures are further investigated. Based on the exchange energy, defined as the difference between the FM and AFM states in a $(2 \times 2)$ supercell with four Mn atoms, *i.e.*, $E_{ex} = E_{AFM} - E_{FM}$. As shown in Table 1, the results demonstrate that $MnTe_2$/Sb has an $E_{ex}$ of 278.6 meV, which is significantly larger than the $E_{ex}$ calculated for monolayer $MnTe_2$ at 146.6 meV, indicating that coupling monolayer $MnTe_2$ with a Sb monolayer not only enhances the perpendicular magnetic anisotropy but also strengthens the FM coupling. The exchange energies ($E_{ex}$) of $MnTe_2$/As and $MnTe_2$/Bi are approximately 49.8 meV and 160.6 meV, respectively.

Using the Heisenberg model, perform Monte Carlo simulations to determine the Curie temperature and magnetic phase diagram of monolayer $MnTe_2$ and the $MnTe_2$/X heterostructures. Consider the classical spin Hamiltonian as[25,54,55]

$$H = -\sum_{i<j} J_{ij} S_i \times S_j - \sum_i A\left(S_i^z\right)^2. \quad (1)$$

where $J_{ij}$ is the exchange coupling constant. $S_i$ refers to the spin operator on $i$-th site, originating from the Mn magnetic moment. $A$ is the single single-ion anisotropy parameter by means of $A = [E_{(100)} - E_{(001)}]/|S|^2$, and $S_i^z$ is the spin component of $i$-th atom along the $z$-direction. Here, we calculate the $J$ values of the nearest-neighbor (NN) Mn atoms. The exchange interactions concerning the Te and X atoms are considered negligible due to their magnetic moments being significantly smaller than that of the Mn atoms. Using the same procedure that only considering the NN interaction, the estimated $T_C$ of the $CrX_3$ (X = Cl, Br, and I) monolayers are 11 K, 22 K and 43 K in sequence,[56] which agree with the experimental measurement of 17 K, 27 K and 45 K.[16,57] The $J$ values can be given by $E_{ex} = E_{AFM} - E_{FM} = 16JS_iS_j$, where $E_{FM} = 12JS_iS_j$, $E_{AFM} = -4JS_iS_j$. The estimated exchange parameters ($J$) and the magnetic transition temperatures ($T_C$) are shown in Table 1 and Fig. 6, respectively. The $MnTe_2$/Sb heterostructure has the largest $T_C$ of 233.2 K. We have also considered three different magnetic configurations (FM, z-AFM, and s-AFM, as shown in Fig. 2) to calculate the exchange coupling constants $J'$ for the next-nearest neighbor Mn atoms. The results reveal that $J'$ is much smaller than $J$. For example, in the case of $MnTe_2$/Sb, the $J$ and $J'$ values are 4.06 meV and 0.32 meV, respectively. The magnetic behavior is predominantly controlled by the NN spin exchange interactions, with next-nearest neighbor effects playing a comparatively lesser role.

Compared with monolayer $MnTe_2$, why do the magnetic coupling and the Curie temperature exhibit an increase in $MnTe_2$/Sb, whereas they experience a reduction in $MnTe_2$/As? On the one hand, the variation can be attributed to strain effects. In $MnTe_2$/As, the $MnTe_2$ layer experiences compressive strain. Conversely, in $MnTe_2$/Sb, the $MnTe_2$ layer undergoes tensile strain. The strain-induced switch between FM and AFM exchange coupling can be qualitatively explained by the expression:[44,54] $J = J_{FM} + J_{AFM} = J_{FM} - 2t^2/U$, which is widely used to describe the balance between FM and AFM exchange interactions. The exchange constant ($J$) comprises both FM and AFM components. The FM term ($J_{FM}$) signifies the direct exchange interaction and strengthens with the increase of exchange integral, which correlates with an augmentation in the overlap density. The AFM term ($J_{AFM}$) is inversely related to the on-site Coulomb repulsion ($U$) and is proportional to the square of the hopping integral ($t$). Increasing $t$ typically associated with decreasing inter-atomic distances, reinforces the AFM exchange. As a crude rule, the AFM exchange coupling is more likely at small inter-atomic distances, while the FM coupling is favorable at intermediate distances. At very large inter-atomic distances, magnetic order tends to be absent. With this understanding, the compressive strain imposed on the $MnTe_2$ layer in $MnTe_2$/As shortens the inter-atomic distance between Mn atoms, enhancing the AFM coupling and thus lowering the overall magnetic exchange interaction ($J$), leading to a decreased

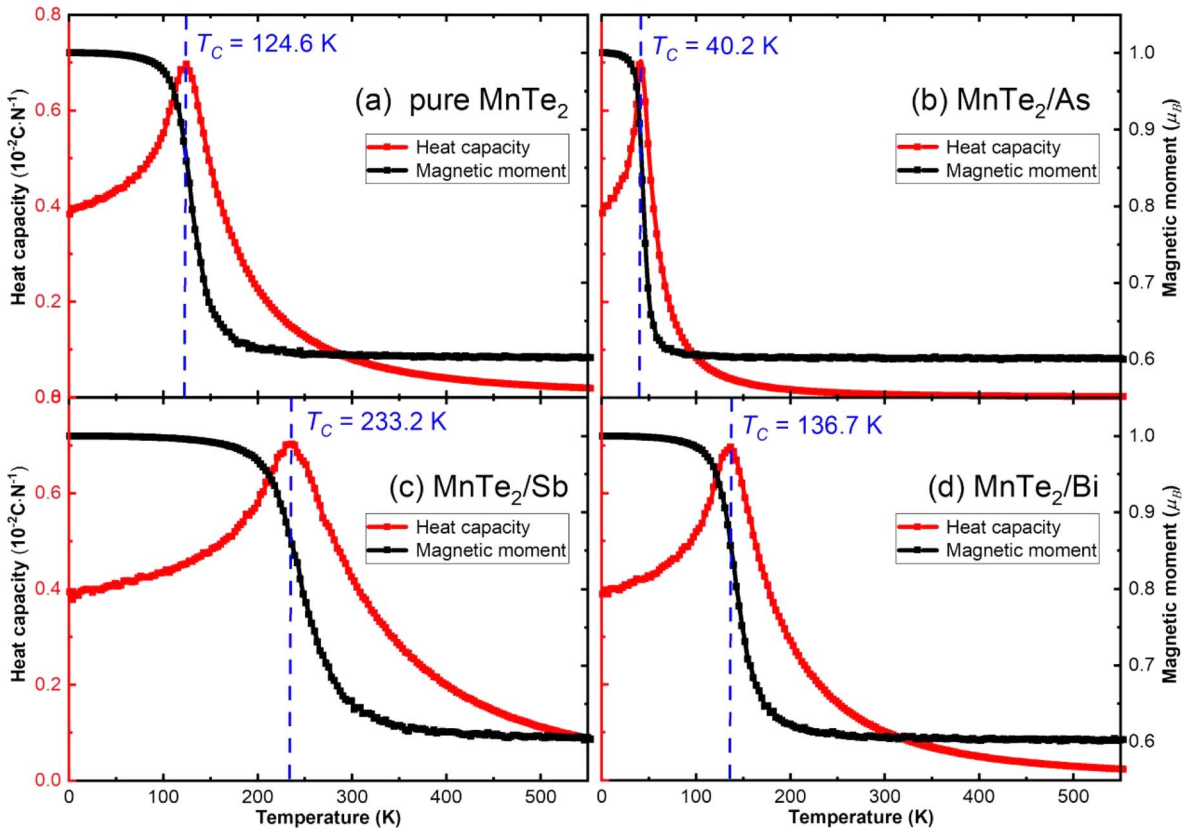


Fig. 6 Magnetic moment and specific heat capacity as a function of temperature for (a) pure $MnTe_2$, (b) $MnTe_2$/As, (c) $MnTe_2$/Sb and (d) $MnTe_2$/Bi *via* Monte Carlo simulations.

$T_C$. In contrast, the $MnTe_2$ layer in $MnTe_2$/Sb subjected to tensile strain exhibit an increased Mn–Mn distance, favoring FM interactions due to more significant overlap of electronic orbitals at intermediate distances. It strengthens the direct exchange mechanism, leading to stronger magnetic coupling and a raised $T_C$. On the other hand, the interfacial coupling and the magnetic interaction pathways are crucially important. For $MnTe_2$/As, As atoms do not significantly contribute to magnetic interactions because they exhibit negligible magnetic moments, suggesting weak coupling with the Mn atoms, then they won't have a substantial impact on $T_C$. In contrast, in $MnTe_2$/Sb, the magnetic moment of the Sb atoms cannot be ignored. The exchange interaction exists not only between Te and Mn atoms but also between Sb and Mn atoms, indicating the existence of additional super-exchange pathways, which can further enhance the magnetic coupling and increase $T_C$. Thirdly, the impact of the SOC effect is an important consideration, as it can influence MAE, which in turn affects the stability of the magnetic moment orientations. Although MAE is not the determining factor for $T_C$, an increase in MAE could contribute to the thermal stability of the magnetization. It is essential to underline that these explanations are simplified models that capture some of the primary physical mechanisms involved. To fully understand these competing mechanisms, detailed computational modeling or experimental studies are necessary.

## IV. Conclusions

In summary, we have investigated the structural and magnetic properties of $MnTe_2$/X (X = As, Sb, and Bi) heterostructures using first-principles calculations. Structural optimization reveals that monolayer $MnTe_2$ forms weak van der Waals interactions with the monolayer of As or Sb. In contrast, interaction with a Bi monolayer leans towards the creation of heterostructures with stronger covalent interactions, marked by the formation of Bi–Te covalent bonds. Notably, joining monolayer $MnTe_2$ with a monolayer of As, Sb, or Bi significantly tunes the MAE. Coupling with monolayer As reorients the easy-magnetization axis from out-of-plane in $MnTe_2$ to in-plane in $MnTe_2$/As, while coupling with monolayer Sb obtain a large perpendicular MAE, reaching as high as 4.13 meV per cell in $MnTe_2$/Sb. The configuration of the vdW heterostructures predominantly revises the SOC matrix element differential of the Te atoms, which in turn dictates the magnetic anisotropy. For $MnTe_2$/Bi, we also observed an in-plane MAE, which is significantly contributed by both Te and Bi atoms. This indicates the considerable role played by heavy element in steering magnetic anisotropy through SOC. Moreover, the coupling of the $MnTe_2$ and X monolayers notably impacts the magnetic interactions, attributable to strain in the $MnTe_2$ layer within the heterostructure and the magnetic proximity effects between the layers. The magnetic exchange energy and Curie temperature of $MnTe_2$/As are both diminished relative to monolayer $MnTe_2$. In contrast, $MnTe_2$/Sb displays a significant enhanced FM coupling and an increased Curie temperature. Our studies provide a deep insight into the magnetic properties of $MnTe_2$/Group VA semiconductor heterostructures.

## Data availability

All relevant data are within the paper.

## Conflicts of interest

The authors declare no competing financial interest.

## Acknowledgements

This work was supported by the Hunan Provincial Natural Science Foundation of China (2023JJ40074), Hunan Provincial Department Project (21B0757, 22B0821, 202401001507), Hunan Engineering Technology Research Center project (2022TP2051, 2022TP2036), Natural Science Foundation of Shandong Province of China (ZR2022MF290).

## References

1 B. Huang, G. Clark, E. Navarro-Moratalla, D. R. Klein, R. Cheng, K. L. Seyler, D. Zhong, E. Schmidgall, M. A. McGuire, D. H. Cobden, W. Yao, D. Xiao, P. Jarillo-Herrero and X. D. Xu, *Nature*, 2017, **546**, 270–273.
2 A. Bedoya-Pinto, J. R. Ji, A. K. Pandeya, P. Gargiani, M. Valvidares, P. Sessi, J. M. Taylor, F. Radu, K. Chang and S. S. P. Parkin, *Science*, 2021, **374**, 616–620.
3 W. O. Chen, Z. Y. Sun, Z. J. Wang, L. H. Gu, X. D. Xu, S. W. Wu and C. L. Gao, *Science*, 2019, **366**, 983–987.
4 C. Gong, L. Li, Z. L. Li, H. W. Ji, A. Stern, Y. Xia, T. Cao, W. Bao, C. Z. Wang, Z. Q. Qiu, R. J. Cava, S. G. Louie, J. Xia and X. Zhang, *Nature*, 2017, **546**, 265–269.
5 Y. J. Deng, Y. J. Yu, Y. C. Song, J. Z. Zhang, N. Z. Wang, Z. Y. Sun, Y. F. Yi, Y. Z. Wu, S. W. Wu, S. W. Zhu, J. Wang, X. H. Chen and Y. B. Zhang, *Nature*, 2018, **563**, 94–99.
6 Z. Y. Fei, B. Huang, P. Malinowski, W. B. Wang, W. B. Song, J. Sanchez, W. Yao, D. Xiao, X. Y. Zhu, A. F. May, W. D. Wu, D. H. Cobden, J. H. Chu and X. D. Xu, *Nat. Mater.*, 2018, **17**, 778–782.
7 A. Bafekry, M. Faraji, M. M. Fadlallah, A. B. Khatibani, A. A. Ziabari, M. Ghergherehchi, S. Nedaei, S. F. Shayesteh and D. Gogova, *Appl. Surf. Sci.*, 2021, **559**, 149862.
8 K. Chen, W. Q. Tang, M. M. Fu, X. Li, C. M. Ke, Y. P. Wu, Z. M. Wu and J. Y. Kang, *Nanoscale Res. Lett.*, 2021, **16**, 104.
9 W. Chen, J. M. Zhang, X. G. Wang, Q. L. Xia, Y. Z. Nie and G. H. Guo, *J. Magn. Magn. Mater.*, 2021, **518**, 167433.
10 Y. C. Cheng, Z. Y. Zhu, W. B. Mi, Z. B. Guo and U. Schwingenschlögl, *Phys. Rev. B: Condens. Matter Mater. Phys.*, 2013, **87**, 100401.
11 X. J. Dong, J. Y. You, B. Gu and G. Su, *Phys. Rev. Appl.*, 2019, **12**, 014020.
12 Z. Y. Guan and S. Ni, *ACS Appl. Electron. Mater.*, 2021, **3**, 3147–3157.
13 Z. Y. Guan and S. Ni, *J. Phys. Chem. C*, 2021, **125**, 16700–16710.
14 H. Y. Lv, W. J. Lu, X. Luo, X. B. Zhu and Y. P. Sun, *Phys. Rev. B*, 2019, **99**, 134416.

15 T. O. Wehling, A. I. Lichtenstein and M. I. Katsnelson, *Phys. Rev. B: Condens. Matter Mater. Phys.*, 2011, **84**, 235110.
16 B. Huang, G. Clark, D. R. Klein, D. Macneill, E. Navarro-Moratalla, K. L. Seyler, N. Wilson, M. A. Mcguire, D. H. Cobden and X. Di, *Nat. Nanotechnol.*, 2018, **13**, 544–548.
17 S. W. Jiang, J. Shan and K. F. Mak, *Nat. Mater.*, 2018, **17**, 406–410.
18 N. Wang, H. Tang, M. Shi, H. Zhang and X. Chen, *J. Am. Chem. Soc.*, 2019, **141**, 17166–17173.
19 K. S. Novoselov, A. Mishchenko, A. Carvalho and A. H. C. Neto, *Science*, 2016, **353**, aac9439.
20 Y. Liu, N. O. Weiss, X. D. Duan, H. C. Cheng, Y. Huang and X. F. Duan, *Nat. Rev. Mater.*, 2016, **1**, 16042.
21 R. Wang, J. Qian, X. Chen, Z. W. Low, Y. Chen, H. Ma, H. A. Wu, C. M. Doherty, D. Acharya and Z. Xie, *Nat. Commun.*, 2023, **14**, 2161.
22 J. Li, X. D. Yang, Y. Liu, B. L. Huang, R. X. Wu, Z. W. Zhang, B. Zhao, H. F. Ma, W. Q. Dang, Z. Wei, K. Wang, Z. Y. Lin, X. X. Yan, M. Z. Sun, B. Li, X. Q. Pan, J. Luo, G. Y. Zhang, Y. Liu, Y. Huang, X. D. Duan and X. F. Duan, *Nature*, 2020, **579**, 368–374.
23 L. M. Zhang, X. Y. Huang, H. W. Doi, M. S. Wang, H. Cheng, L. Tong, Z. Li, X. T. Han, X. Wang, L. Ye and J. B. Han, *Adv. Mater.*, 2020, **32**, 2002032.
24 S. B. Chen, C. X. Huang, H. S. Sun, J. F. Ding, P. Jena and E. J. Kan, *J. Phys. Chem. C*, 2019, **123**, 17987–17993.
25 X. M. Xu, Z. P. Sun, X. H. Wang, Z. R. Gao, L. X. Guan, S. Zhang, P. Chang and J. G. Tao, *Appl. Surf. Sci.*, 2022, **572**, 151478.
26 J. J. Liao, Y. Z. Nie, X. G. Wang, Z. Y. Luo, Q. L. Xia, R. Xiong and G. H. Guo, *Phys. Rev. B*, 2023, **107**, 184403.
27 S. X. Qu, A. L. Li, N. Jiang, D. H. Zhang and F. P. Ouyang, *J. Phys. D Appl. Phys.*, 2022, **55**, 394005.
28 J. J. Liao, Y. Z. Nie, X. G. Wang, Z. Y. Luo, Q. L. Xia, R. Xiong and G. H. Guo, *Phys. B*, 2024, **675**, 415642.
29 Q. Q. Wu, J. Wang, T. Zhi, Y. L. Zhuang, Z. K. Tao, P. F. Shao, Q. Cai, G. F. Yang, J. J. Xue, D. J. Chen and R. Zhang, *Nanotechnology*, 2024, **35**, 305204.
30 W. Y. Zhou, A. J. Bishop, X. S. Zhang, K. Robinson, I. Lyalin, Z. L. Li, R. Bailey-Crandell, T. M. J. Cham, S. Y. Cheng, Y. K. Luo, D. C. Ralph, D. A. Muller and R. K. Kawakami, *Phys. Rev. Mater.*, 2023, **7**, 104004.
31 J. L. Yang, X. Y. Wang, S. J. Li, X. A. Wang, M. H. Pan, M. Z. Ai, H. Yuan, X. N. Peng, R. L. Wang, Q. Li, F. W. Zheng and P. Zhang, *ACS Nano*, 2023, **17**, 23160–23168.
32 Y. L. Gao, Q. X. Liu, X. Jiang and J. J. Zhao, *Appl. Phys. Lett.*, 2022, **121**, 162402.
33 H. Idzuchi, A. E. L. Allcca, X. C. Pan, K. Tanigaki and Y. P. Chen, *Appl. Phys. Lett.*, 2019, **115**, 232403.
34 X. J. Dong, J. Y. You, Z. Zhang, B. Gu and G. Su, *Phys. Rev. B*, 2020, **102**, 144443.
35 Y. P. Qi, P. G. Naumov, M. N. Ali, C. R. Rajamathi, W. Schnelle, O. Barkalov, M. Hanfland, S. C. Wu, C. Shekhar, Y. Sun, V. Süss, M. Schmidt, U. Schwarz, E. Pippel, P. Werner, R. Hillebrand, T. Förster, E. Kampert, S. Parkin, R. J. Cava, C. Felser, B. H. Yan and S. A. Medvedev, *Nat. Commun.*, 2016, **7**, 11038.
36 X. Y. Ma, T. Dai, S. Dang, S. D. Kang, X. X. Chen, W. Q. Zhou, G. L. Wang, H. W. Li, P. Hu, Z. H. He, Y. Sun, D. Li, F. M. Yu, X. Zhou, H. J. Chen, X. M. Chen, S. X. Wu and S. W. Li, *ACS Appl. Mater. Interfaces*, 2019, **11**, 10729–10735.
37 Y. J. Wang, E. F. Liu, H. M. Liu, Y. M. Pan, L. Q. Zhang, J. W. Zeng, Y. J. Fu, M. Wang, K. Xu, Z. Huang, Z. L. Wang, H. Z. Lu, D. Y. Xing, B. G. Wang, X. G. Wan and F. Miao, *Nat. Commun.*, 2016, **7**, 13142.
38 H. F. Ma, P. Chen, B. Li, J. Li, R. Q. Ai, Z. W. Zhang, G. Z. Sun, K. K. Yao, Z. Y. Lin, B. Zhao, R. X. Wu, X. W. Tang, X. D. Duan and X. F. Duan, *Nano Lett.*, 2018, **18**, 3523–3529.
39 Q. Q. Liu, F. C. Fei, B. Chen, X. Y. Bo, B. Y. Wei, S. Zhang, M. H. Zhang, F. J. Xie, M. Naveed, X. G. Wan, F. Q. Song and B. G. Wang, *Phys. Rev. B*, 2019, **99**, 155119.
40 H. Y. Lv, W. J. Lu, D. F. Shao, Y. Liu and Y. P. Sun, *Phys. Rev. B: Condens. Matter Mater. Phys.*, 2015, **92**, 134416.
41 J. Li, B. Zhao, P. Chen, R. X. Wu, B. Li, Q. L. Xia, G. H. Guo, J. Luo, K. T. Zang, Z. W. Zhang, H. F. Ma, G. Z. Sun, X. D. Duan and X. F. Duan, *Adv. Mater.*, 2018, **30**, 1801043.
42 X. L. Sui, T. Hu, J. F. Wang, B. L. Gu, W. H. Duan and M. S. Miao, *Phys. Rev. B*, 2017, **96**, 041410(R).
43 C. Ataca, H. Sahin and S. Ciraci, *J. Phys. Chem. C*, 2012, **116**, 8983–8999.
44 W. Chen, J. M. Zhang, Y. Z. Nie, Q. L. Xia and G. H. Guo, *J. Phys. Chem. Solids*, 2020, **143**, 109489.
45 W. Chen, J. M. Zhang, Y. Z. Nie, Q. L. Xia and G. H. Guo, *J. Magn. Magn. Mater.*, 2020, **508**, 166878.
46 S. Zhang, M. Xie, F. Li, Z. Yan, Y. Li, E. Kan, W. Liu, Z. Chen and H. Zeng, *Angew. Chem., Int. Ed.*, 2016, **55**, 1666–1669.
47 C. Chen, Z. Song, J. Z. Zhao, Z. Y. Chen, Z. M. Yu, X. L. Sheng and S. Y. A. Yang, *Phys. Rev. Lett.*, 2020, **125**, 056402.
48 M. U. Rehman, X. L. Dong, T. Hou, Z. Y. Li, S. F. Qi and Z. H. Qiao, *Phys. Rev. B*, 2019, **100**, 195422.
49 W. Kohn and L. Sham, *Phys. Rev.*, 1965, **140**, A1133.
50 P. E. Blchl, *Phys. Rev. B: Condens. Matter Mater. Phys.*, 1995, **50**, 17953–17979.
51 J. P. Perdew, K. Burke and M. Ernzerhof, *Phys. Rev. Lett.*, 1996, **77**, 3865.
52 M. Kan, J. Zhou, Q. Sun, Y. Kawazoe and P. Jena, *J. Phys. Chem. Lett.*, 2013, **4**, 3382–3386.
53 M. Kan, S. Adhikari and Q. Sun, *Phys. Chem. Chem. Phys.*, 2014, **16**, 4990–4994.
54 H. J. Xiang, C. Lee, H. J. Koo, X. G. Gong and M. H. Whangbo, *Dalton Trans.*, 2013, **42**, 823–853.
55 W. Chen, P. D. Zhu, H. Liu, Z. J. Zhu, Q. X. Zheng, H. B. Chen, H. Y. Yi, J. J. Liao and G. H. Guo, *J. Mater. Chem. C*, 2024, **12**, 2756–2763.
56 K. Sheng, H. K. Yuan and Z. Y. Wang, *J. Mater. Chem. C*, 2021, **9**, 16495–16505.
57 K. Hyun Ho, Y. Bowen, L. Siwen, J. Shengwei, J. Chenhao, T. Zui, N. George, S. Francois, Z. Shazhou and L. Chenghe, *Proc. Natl. Acad. Sci. U. S. A.*, 2019, **116**, 11131–11136.